

ARTICLE OPEN



An integrated and robust plant pulse monitoring system based on biomimetic wearable sensor

Chao Zhang¹, Chi Zhang¹, Xinyue Wu¹, Jianfeng Ping¹ and Yibin Ying¹

Plant wearable sensors have potential to provide continuous measurements of plant physiological information. However, stable and high-fidelity monitoring of plants with glandular hairs and wax is challenging, due to lacking interface adaptability of conventional plant wearable sensors. Here, inspired by adaptive winding plant tendrils, an integrated plant wearable system (IPWS) based on adaptive winding strain (AWS) sensor for plant pulse monitoring was developed. The IPWS consists of three modules, i.e. an AWS sensor, a flexible printed circuit, and a smart phone APP display interface. As the key element, the AWS sensor can adaptively wrap around the tomato stem. Importantly, with the serpentine-patterned laser-induced graphene, the AWS sensor exhibits excellent resistance to temperature interference with a temperature resistance coefficient of 0.17/°C. The IPWS is demonstrated to be stable and high-fidelity monitoring the plant pulse, which can reflect the growth and water state of tomato plant in real time.

npj Flexible Electronics (2022)6:43; <https://doi.org/10.1038/s41528-022-00177-5>

INTRODUCTION

Communication with silent plants to obtain their growth information is important for mechanism study and improving crop yields^{1–5}. Studies have shown that the process of plant growth is similar to the contraction and expansion of human pulse, which is embodied in the contraction and expansion of the stem during the day and at night^{6–8}. And repeating expansion leads to plant growth. Actually, plant pulse is related to the absorption and transpiration of water by plants^{8–10}. During the day, when most stomata on leaves are open and the transpiration of water from leaves is greater than the absorption of water by roots, the stem diameter barely changes or shrinks. At night, when the stomata on leaves are closed, the plant absorbs more water from roots than water evaporation from leaves, and the stem will expand. When water is scarce, the stem shrinks obviously. Therefore, monitoring plant pulse can understand the relationship between plant growth and water supply.

Currently, the sensors applied for plant pulse monitoring are mainly rigid linear variable transducer (LVDT) sensors¹¹. Bulky and heavy LVDT sensors are difficult to fix and have pre-tightening force on plants⁸, which is not suitable for plant seedling monitoring since the growth of plant seedling is fundamental for the fruit setting and yield. Recently, flexible strain sensors that can be worn on plants have appeared the huge potential to continuously measure plant growth^{12–14}. In recent years, several planar strain sensors for plant growth monitoring have been developed^{2–4}. However, there still exists some challenges in the application of planar strain sensors for the plant pulse monitoring. Firstly, the compact glandular hairs and wax on plant stem affect the fixation of wearable planar sensors. Sensors bound to plants by tape are not conducive to the growth of plants and may fall off during the long-term monitoring. In addition, complex environment poses a threat to the sensors' stability¹⁵. Indeed, plant growth environment is complex and changeable, such as changes of light, humidity and temperature, which might lead to the loss of sensors' data fidelity¹⁶. Finally, the wired data acquisition method

has the disadvantages of cumbersome wiring and high cost. To the best of our knowledge, there has been no wearable sensing system with flexible adaptability and excellent anti-interference performance reported for plant pulse monitoring yet. Therefore, it is necessary to develop a plant wearable sensing system with flexible adaptability, anti-interference performance, and wireless data transmission to monitor the plant pulse.

Herein, an integrated plant wearable system (IPWS) based on adaptive winding strain (AWS) sensor for wireless monitoring of plant pulse was developed (Fig. 1a). The IPWS consists of three modules, i.e. an AWS sensor, a flexible printed circuit, and a smart phone APP display interface. The key element, AWS sensor was designed inspired by the plant tendrils, which can adaptively wrap around the tomato stem without any paste or adhesive. This biomimetic tendril structure converts a direct stretching strain into the curvature effect, and avoids the strain deficiency from crack fracture. In addition, the AWS sensor exhibits resistance to temperature interference via the serpentine-patterned design, making the long-time and anti-interference monitoring for plant pulse come true. The expansion and shrink of stem can stimulate the AWS sensor to generate resistance variation, which can be recorded by the IPWS that transmits the resistance variation data to smart phone wirelessly. The results show that the IPWS system can accurately monitor the plant pulse to diagnose the growth and water state of tomato plant.

RESULTS

System design

As shown in Supplementary Fig. 1, there are compact glandular hairs and essential oil on the surface of tomato stem, which is not conducive to the fixation of flexible wearable sensors. Plant tendrils can wrap around the stems of host plants, and the curvature of spiral line automatically varies with the expansion and shrink of plants stem, without affecting the normal growth of the host plants^{17,18}. Studies on plant tendrils prove that the layer

¹Laboratory of Agricultural Information Intelligent Sensing, College of Biosystems Engineering and Food Science, Zhejiang University, 866 Yuhangtang Road, Hangzhou 310058, PR China. ✉email: ybying@zju.edu.cn

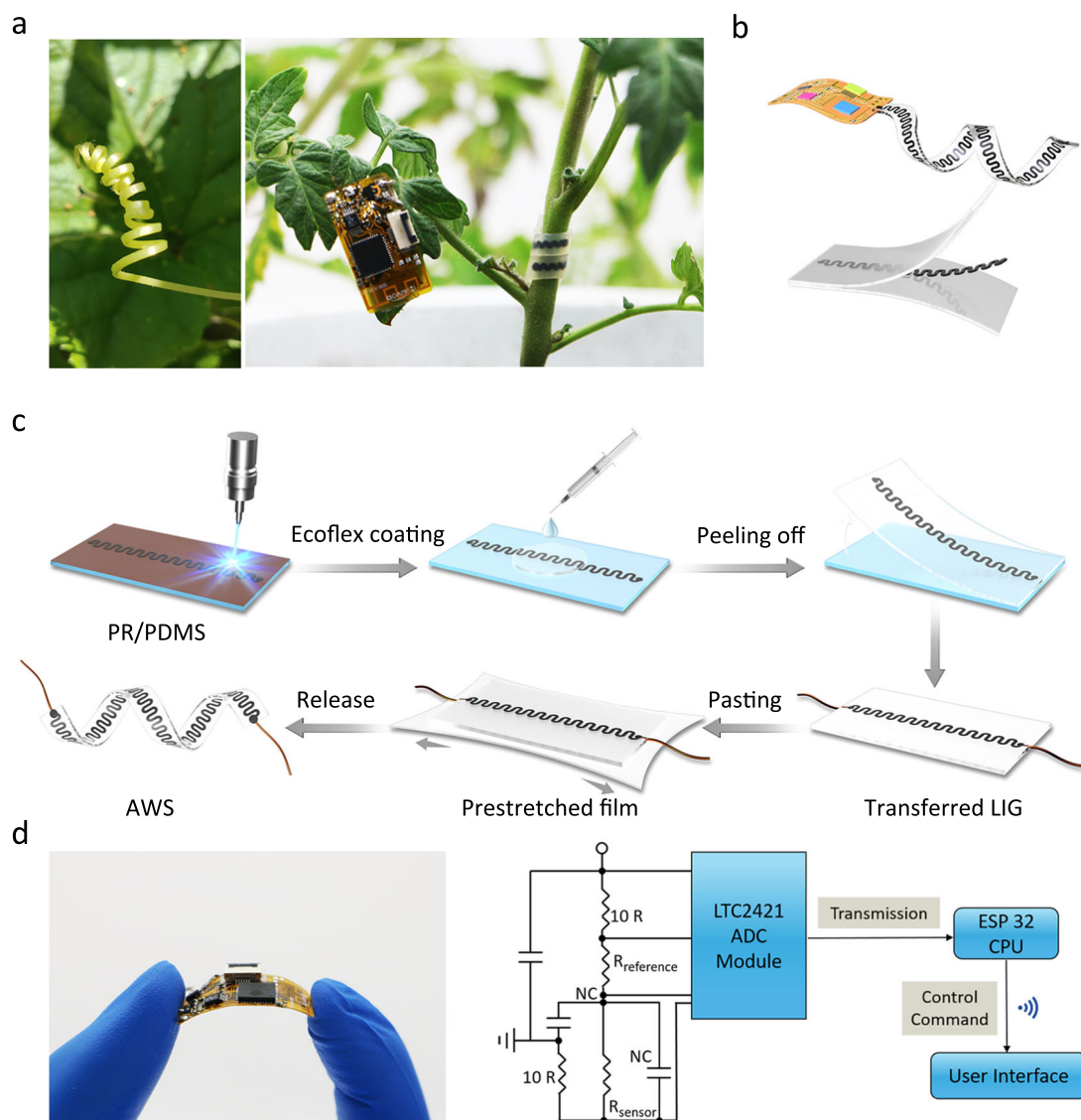


Fig. 1 Schematics of the IPWS for plant pulse monitoring. **a** The optical images of plant tendril and IPWS on tomato seedlings. **b** Schematic diagram of the AWS sensor integrated with the flexible printed circuit. **c** Schematic diagram of the fabrication of AWS sensor. **d** The optical image of bent printed circuit, and schematic illustration of the system-design for the signal transduction, processing and wireless transmission from the AWS sensor to the user interface.

closer to the concave surface of tendrils is higher lignified than that of the other side, which will lead to strain mismatch at the fiber interface and make tendrils curl^{18–20}. According to this mechanism, the plant wearable sensor with a biomimetic tendril structure was designed, which can adaptively wrap around the tomato stem without any fixation devices and tape (Fig. 1a). As shown in Fig. 1b, the AWS is a sandwich structure, with 3D porous laser-induced graphene (LIG) wall sandwiched between transparent Ecoflex layers. The sandwiched LIG layer can convert the strain response to the resistance signal, which can be captured, converted, and transmitted by the flexible printed circuit module. The preparation process of the AWS sensor is shown in Fig. 1c. There are two significant strategies. Firstly, it is the transfer of patterned LIG from polydimethylsiloxane (PDMS) to Ecoflex. We prepared the 3D porous LIG wall on the Polyethylene terephthalate (PET), glass, polystyrene, and PDMS substrates, respectively. Then Ecoflex was applied to transfer the LIG. As shown in Supplementary Fig. 2, the results showed that the LIG on the first three substrates could not be completely transferred, and only the LIG on the PDMS substrate could be transferred completely. This is

due to the low surface energy of PDMS ($\approx 30 \text{ mN m}^{-1}$)^{21–23}, which provides a non-adhesive substrate for stripping LIG²⁴. This strategy can transfer precise LIG patterns in a large scale (Supplementary Fig. 3). Secondly, the transferred patterned LIG is flipped and attached to the surface of another prestretched Ecoflex film. After releasing the prestretched film, the mismatched strain between the upper and lower interfaces makes the composite polymer film automatically curl into a tendril structure with specific curvature. The curvature of spiral structure can be tuned by adjusting the pretrains, which would be discussed in the characterization of electromechanical properties.

Wireless data communication plays an essential role in wearable sensing systems^{25–27}. Wearable wireless sensor systems for human body are often integrated with Bluetooth communication^{28–30}. However, using Bluetooth wireless transmission is impossible to realize remote and large-scale monitoring of plants in the field. Therefore, a flexible printed circuit with WIFI wireless data transmission function was designed and fabricated to realize the wireless communication between AWS sensor and a smart phone. The detailed principle and fabrication process are described in

the methods section and shown in Fig. 1d and Supplementary Fig. 4. As shown in Supplementary Fig. 4, users can view the monitoring data of multiple tomatoes and export data through the mobile phone interface.

Characterizations

We prepared the 3D porous LIG on the phenolic resin (PR) film and transfer the LIG to the Ecoflex film (Figs. 2 and 3). Scanning

electron microscope (SEM) was used to characterize the morphologies of the LIG and transferred LIG. The microstructure of the LIG is mainly determined by laser power and scanning rate (Fig. 2)^{31,32}. The low laser power and fast scanning rate would not provide sufficient energy to formation of graphene (Fig. 2a). If the laser power is too high, the 3D porous graphene structure would be over-burned, resulting in collapse of layer structure and increase the resistance (Fig. 2e). Figure 2b shows that the 3D porous

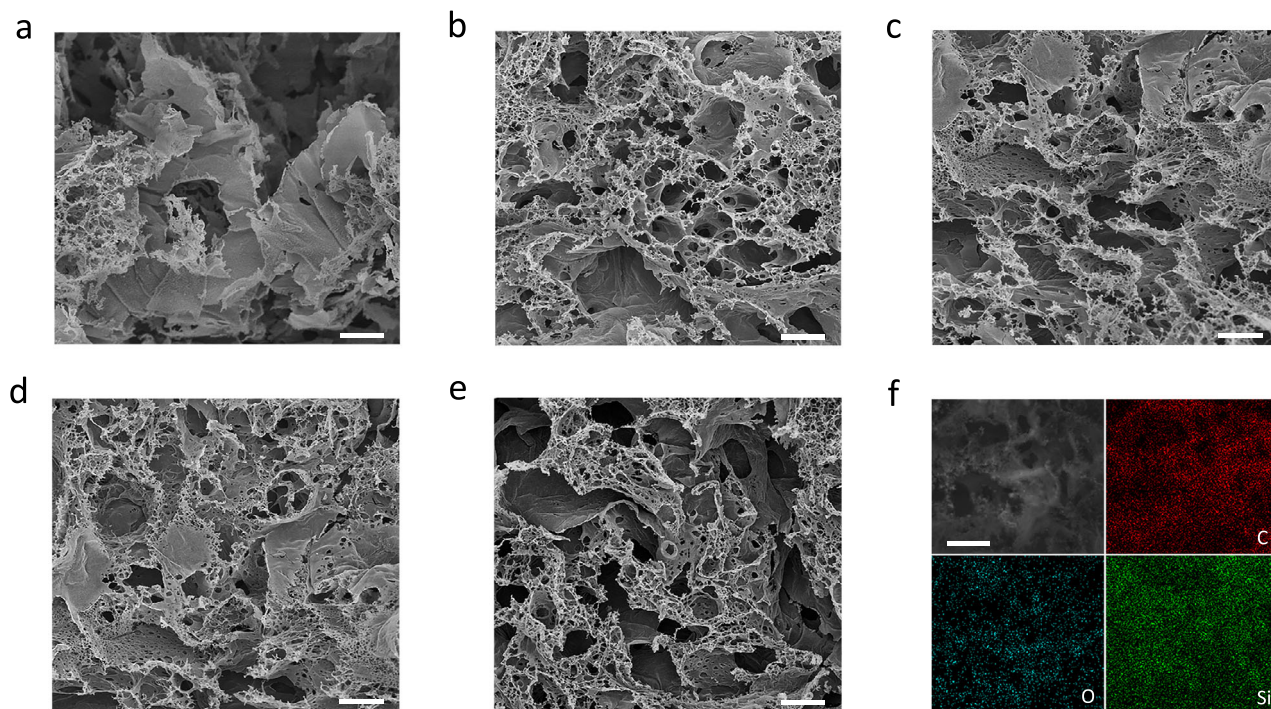


Fig. 2 Morphology characterization of LIG with various laser powers and scanning rates. **a–c** SEM images of LIG prepared by different laser scan speeds (80, 27, and 16 cm s^{-1}) with a laser power of 2.5 W. **d, e** SEM images of LIG prepared with different laser power (2.2 and 2.8 W) with a laser scan speed of 27 cm s^{-1} . **f** SEM image of prepared LIG and the corresponding elemental mapping of C, O, and Si elements. Scale bars: 10 μm .

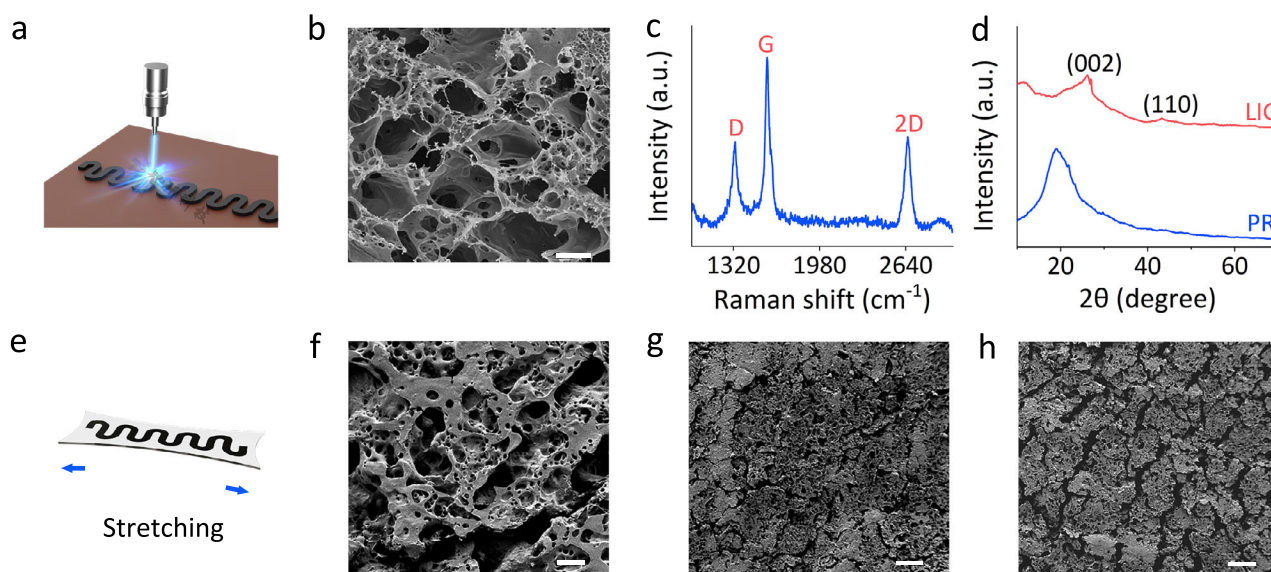


Fig. 3 Morphology characterization of LIG before and after being transferred. **a** The diagram of LIG before being transferred. **b** The SEM image of LIG. **c** The Raman spectrum of LIG. **d** The XRD analysis of LIG. **e** The diagram of transferred LIG. **f, g** The SEM images of transferred LIG. **h** The SEM morphologies of transferred LIG under 5% of strain. Scale bars: **b** = 5 μm , **f** = 20 μm , **g**, **h** = 200 μm .

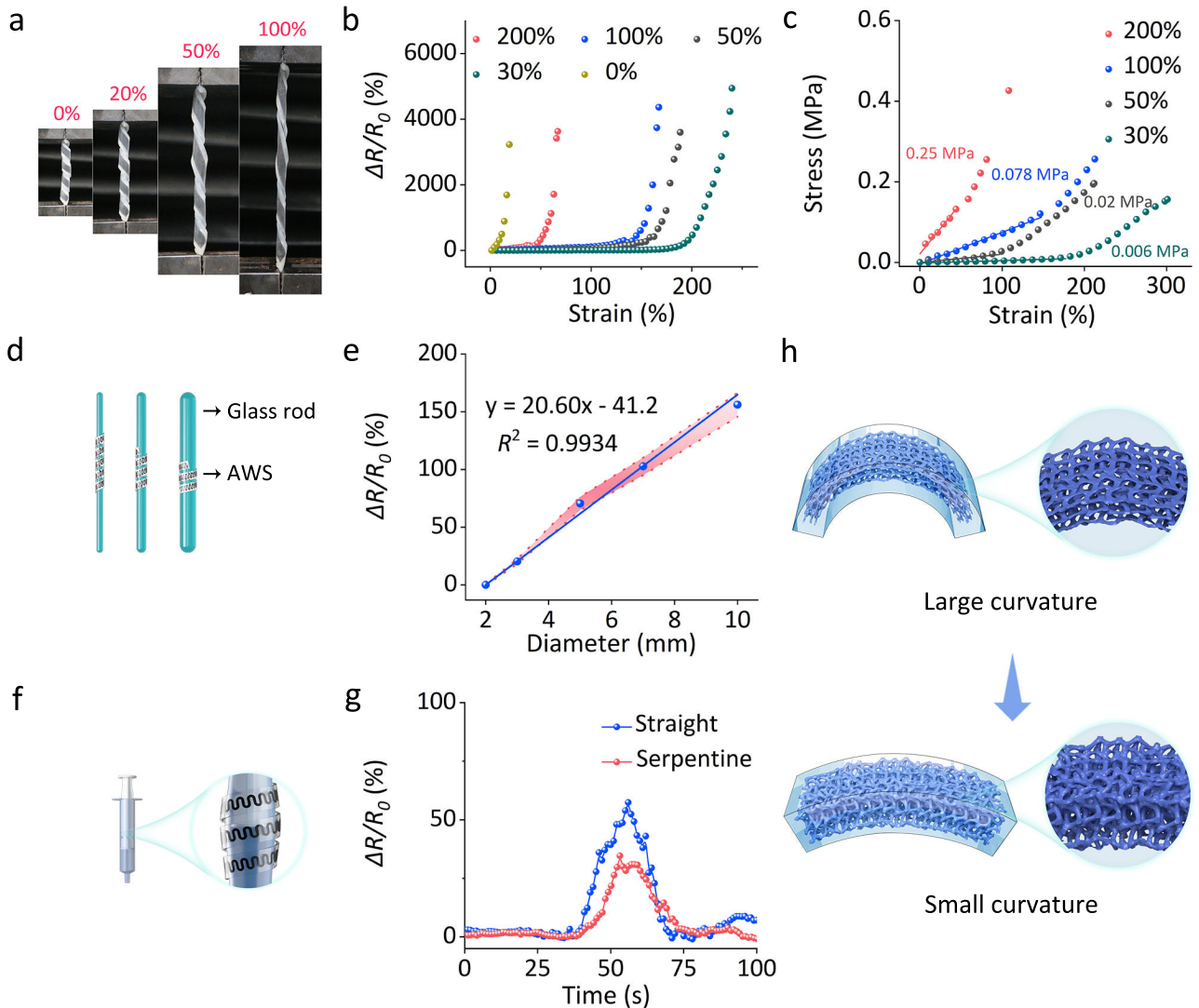


Fig. 4 Electromechanical performance. **a** The optical images of the experimental setup. **b** The relative resistance variation of AWS sensors with different prestrains versus the tensile strain. **c** The elastic modulus (E) of helical structure with different prestrains. **d** Schematic illustration of static simulation using glass rods. **e** The sensor's responses to glass rods with different diameters (2, 3, 5, 7 and 10 mm). **f** Schematic illustration of dynamic simulation using injection syringe. **g** The sensor's responses with dynamic simulation. **h** The schematic illustration of sensing mechanism.

graphene wall structure can be formed under the laser power 2.5 W and scanning rate 27 cm s^{-1} , and these porous structures are formed by the release of gas in the laser transformation process. The uniform 3D porous structure facilitates the penetration of the Ecoflex, and thus it can be fully transferred from the surface of PDMS substrate. After the transferring process, the interconnecting multi-layer LIG sheet structure is reserved, and the silicone rubber inevitably occupies plenty of porous space (Fig. 3f, g). After application of the 5% strain (Fig. 3h), it can be seen that many microcracks consisting of gaps, islands, and bridges connecting separated islands appears on the surface³³. These microcracks cause partial fracture of the original conductive network, which leads to the increased electrical resistance and strain response^{34,35}.

The Raman spectrum is a golden characterization technique for carbon materials, which is extremely sensitive to geometric structure and bonding within molecules^{36,37}. As shown in Fig. 3c, LIG exhibits three typical Raman peaks of graphene, including D band at 1335 cm^{-1} , G band at 1582 cm^{-1} , and 2D band at 2659 cm^{-1} , whereas D band is corresponding to the structural defects in graphene, and the G band is related to the graphite

carbon E2g pattern^{36,38,39}. The low I_D/I_G ratio of 0.52 reveals the highly crystalline structure of graphene^{40–42}. The obvious 2D band reveals the formation of 3D multilayer graphene structures⁴³. The X-ray diffraction (XRD) patterns of the LIG and PR are shown in Fig. 3d. The characteristic peak of PR is at 19.1° , while there is hardly any characteristic peak of the PR in Raman spectrum of the LIG. There are typical graphitic crystal phase (002) and (100) peaks at 26.1° and 43.4° , respectively^{32,44}. These results further confirm the formation of the graphene structure.

Electromechanical properties of the AWS sensor (Fig. 4a–c) were investigated via mechanical tensile tests. Similar to the strain of plant tendrils, the strain process of the AWS sensor consists of elastic deformation and plastic deformation⁴⁵. The elastic deformation first occurs during the strain process, followed by the plastic deformation. The LIG structure was torn and finally broke during plastic deformation. As shown in Fig. 4b, the effect of different prestrains (0%, 30%, 50%, 100% and 200%) on the effective strain sensing ranges of the AWS sensor was investigated. Compared with the strain sensing range of planar sensor (0% prestrain), the ASW sensors (30%–200% prestrains) show

higher effective strain sensing ranges. For the prestrain increases from 30% to 200%, the strain sensing range decrease from 240% to 66%. This is because the larger prestrain results in more helices with smaller curvature, which leads to the decrease of elastic deformation range and the earlier occurrence of plastic deformation (Supplementary Fig. 5a). Therefore, the mechanical properties of the spiral structure can be tuned by prestrain. The specific mechanism can be explained by the tendril curvature expression¹⁹:

$$k = \frac{6\varepsilon(1+m)^2}{(t_1+t_2)\left[3(1+m)^2+(1+mn)\left(m^2+\frac{1}{mn}\right)\right]} \quad (1)$$

Where ε is prestrain, and t_1 and t_2 are the thickness of the upper and lower Ecoflex film, respectively. And $m = t_1/t_2$, and $n = E_1/E_2$ (E_1 and E_2 are the young's modulus of the upper and lower Ecoflex film, respectively). In this study, the t_1 , t_2 , E_1 , E_2 , m and n are constant. Therefore, the initial curvature of the tendril is mainly determined by the prestrain. The effects of prestrain on the elastic modulus (E) of helical structure was evaluated (Fig. 4c). The slope of the approximate linear part of the strain-stress curve is the elastic modulus of tendril obtained⁴⁵. The results show that in the prestrain range of 30% to 200%, the elastic modulus increases as the prestrain increases. The elastic modulus corresponding to 30%, 50% and 100% of prestrain is 0.006, 0.02, and 0.078 MPa, which is far less than the turgor of plant cells (0.2–1.0 MPa)⁴⁶. Therefore, the pretension generated by the AWS sensor wrapped around the stem of plants will not affect the normal growth of plants. Supplementary Fig. 5b shows the reversible response of the AWS sensor (Prepared under prestrain of 100%, and its effective strain is about 150%) under various strains from 1% to 100%. For different strains, the sensor displays reversible and increased responses with the increase of strain (The impurity peak of 1% and 5% might be caused by the vibration from the sudden stop of fixture). In addition, the repeated responses of the sensor were recorded with strains of 60% for 8000 s (Supplementary Fig. 5c), and the sensor remains stable and exhibits excellent durability. A downward drift in peak value of the resistance variation rate ($\Delta R/R_0$) was observed in initial few cycles. This might be due to the construction of new conductive networks and subsequent formation of an equilibrium state of the conductive networks during the cyclic loading and unloading⁴⁷.

Sensing mechanism

In this study, the sensing mechanism of the AWS sensor was investigated by using static simulation (Fig. 4d, e) and dynamic simulation (Fig. 4f, g) methods. The relative mechanism is exhibited in Fig. 4h. The sensor's responses to glass rods with different diameters (2, 3, 5, 7 and 10 mm) were investigated in the static simulation (Fig. 4d). As shown in Fig. 4e, the resistance variation rate increases with the increase of the glass rod diameter, and there is a good linear relationship between the resistance variation rate of the sensor and the glass rod diameter ($R^2 = 0.9934$). This is likely to be that the decreasing glass rod diameter leads to the increasing of sensor's curvature, and 3D porous graphene structure is more compressed (Fig. 4h). In the dynamic simulation, a 5 mL syringe wrapped with AWS sensor was fixed on an automatic sample injection pump. The injection pump slowly pushed the syringe piston. When the piston passed, a tiny expansion about 100 μm occurred (Fig. 4f). As a result, the expansion leads to the decrease of curvature, and parts of the compressed 3D porous graphene structure is released, which increases the electrical resistance (Fig. 4h). The responses of the straight-patterned graphene sensor and the serpentine-patterned sensor are compared (Fig. 4g), and it is found that the serpentine-patterned one is less sensitive than that of straight-patterned one,

which is due to that the serpentine structure can absorb the strain caused by the mechanical deformation⁴⁸.

Anti-environmental interference performance

The growth of plants requires specific environmental conditions, such as adequate light, appropriate humidity, and temperature differences. Therefore, unlike other wearable sensors for animals and human beings, the impact of environmental factors on the performance of plant wearable sensors must be considered. In this study, the influence of temperature, humidity, and light on the sensor performance were investigated. The AWS sensor wrapped around on a glass rod and was tested in an artificial climate box.

When the temperature rises, the thermal expansion of Ecoflex film results in the formation of microcracks in the conductive network, which lengthens the conductive channels, and increases the electrical resistance (Fig. 5a). In order to enhance sensor's temperature resistance, the LIG pattern is designed to be serpentine for AWS sensor, since the serpentine structure can absorb the strain caused by the thermal expansion of the Ecoflex film^{48,49}. As shown in Fig. 5b, compared with the straight-patterned AWS sensor, serpentine-patterned AWS sensor exhibits higher thermal stability. Typically, greenhouse crops, such as tomatoes, grow at temperatures from 15 to 30 °C. In the range of 15–30 °C, the temperature coefficient of resistance (TCR) is applied to estimate sensor's resistance to temperature. The TCR can be obtained by the formula:

$$TCR = \frac{1}{R(T_0)} \frac{R(T) - R(T_0)}{T - T_0} \quad (2)$$

Where $R(T)$ and $R(T_0)$ are the resistance at 30 °C and 15 °C, respectively. The results show that the TCR of the serpentine-patterned AWS sensor is 0.17/°C, which is much less than that of straight-patterned AWS sensor (1.15/°C). Therefore, the serpentine-patterned design can be used to reduce the temperature interference to the AWS sensor. As shown in Fig. 5c, d, in the humidity range of 55–65% and illumination range of 0–8 klx, both the resistance responses of two patterned sensors are not interfered. All these demonstrate that the AWS sensor with serpentine-patterned LIG possesses excellent anti-interference ability, which is significant for plant wearable sensor to monitor plant behavior under complex field conditions.

In vivo monitoring of plant pulse

As shown in Fig. 6a, the AWS sensor can adaptively wrap around the tomato stem without any paste or adhesive. When the transpiration rate of plant is higher than the water absorption rate of root, the stem shrinks. Instead, the stem expands. Therefore, the pulse of tomato can be used to reflect the water status. By incorporating the AWS sensor into the IPWS, the response signal can be transmitted to smart phone wirelessly. A series of tomato seedlings with a height of 25 cm were used for in vivo monitoring. As shown in Fig. 6b, the IPWS was used to monitor the stem diameter variations (SDV) of tomato seeding at 15 cm above the ground. A commercial LVDT sensor as a reference sensor, was used to verify the practicability and accuracy of IPWS. The LVDT sensor was fixed on the tomato seeding stem (at 10 cm above the ground) with rubber band, and kept stable with another holder, which is quite difficult for the tomato seedlings. In addition, the LVDT sensor cannot be fixed on the crooked and tenuous stem. In contrast, the IPWS can be installed simply on any stem of tomato without any rubber band or adhesive tape (Fig. 6b).

The tomato stem was monitored for 11 days by IPWS and reference sensor in an artificial climate box. Figure 6c shows the real-time monitoring curve of SDV within 11 days, with data being recorded every 10 seconds. The overall SDV shows a regularity of

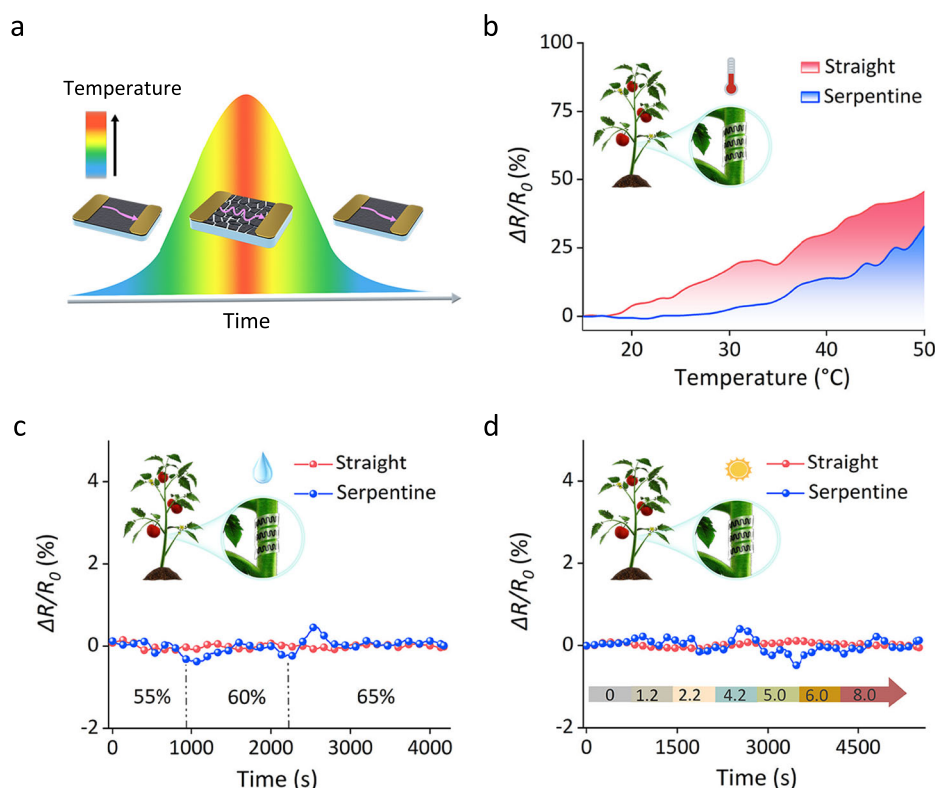


Fig. 5 Anti-environmental interference performance. **a** Schematic of thermal expansion of AWS sensor. **b** The response of straight-patterned AWS sensor and serpentine-patterned AWS sensor at different temperatures. **c** The response of straight-patterned AWS sensor and serpentine-patterned AWS sensor at different humidity (55%, 60%, and 65%). **d** The response of straight-patterned AWS sensor and serpentine-patterned AWS sensor at different illumination intensity (0–8 klx).

pulse with an increasing trend, and IPWS is consistent with the response trend of reference sensor. Taking the monitoring data of the 2nd day as an example (Fig. 6d), the day-night expansion and shrink of tomato stem was investigated. We noticed that the growth time of tomato is mainly at night. In daytime, the SDV and resistance variation rate tends to be stable. This is due to the fact that the transpiration rate of plants is almost equal with the water absorption rate of roots. The SDV and resistance variation rate increases, which is due to the fact that the transpiration rate of the tomato at night is lower than the water absorption rate of roots.

Meanwhile, the soil moisture sensor was used to record the change of relative soil moisture content (RSWC) during the monitoring (Fig. 6e). The initial soil moisture was 50% and dropped to 8% on the 8th day. After watering, the soil moisture was recovered. Combining with the soil moisture, the daily average responses of the two sensors are compared, and the consistent trends are exhibited. It is found that the growth rate of SDV slows down, when the soil moisture is lower than 30%. The closed stomata under the 24% soil moisture also demonstrates the occurrence of drought stress (Supplementary Fig. 6a, b). After soil moisture is recovered, the growth rate of SDV increases, and the stomata opened (Supplementary Fig. 6c, d).

As shown in Fig. 6f, the minimum growth rate of SDV obtained from IPWS and reference sensor is appeared on the 8th day and 9th day, respectively. The difference of minimum growth rate obtained from the IPWS and reference sensor may be caused by the different locations of the sensors. After increasing the soil moisture on the 10th day and 11th day, the growth rate increased. In addition, linear fitting was carried out between the SDV measured by the reference sensor and the resistance variation rate measured by IPWS (Fig. 6g). It is found that there is a good linear relationship between the resistance variation rate and the SDV of

tomato stem ($R^2 = 0.9196$). Therefore, the IPWS can reveal the expansion and shrink of tomato stem to reflect the water status of the tomato.

DISCUSSION

In summary, an IPWS based on AWS sensor for plant pulse monitoring was developed. The AWS sensor can adaptively wrap on the stem without affecting the normal expansion and shrink of the stem due to the biomimetic tendril structure. Importantly, AWS sensor with serpentine-patterned LIG exhibited the enhanced resistance to thermal expansion strain induced by the environmental temperature as compared the one using straight-patterned LIG. Results demonstrate the IPWS can monitor the expansion and shrink of plant stem wirelessly, and reflect the growth and water state of tomato in real time. This work is significant for the continuous monitoring of plant pulse and also provides a reference for development of robust plant wearable sensor. In the future, the sensor should be integrated with cloud computing, and feeds the monitoring information back to precision irrigation equipment to guide agricultural irrigation efficiently.

METHODS

Materials and instruments

Iron (III) chloride (FeCl_3) was purchased from Aladdin (China). The PR was purchased from Shuangfu Plastic Raw Material Co., Ltd (Dongguan, China). The Ecoflex (Smooth on, 0050) was purchased from the Dongzhixuan Co., Ltd (Shanghai, China). The PDMS (Dow Corning) was purchased from Zadok Trading Co., Ltd (Shanghai, China).

The SEM images were obtained from a field-emission scanning electron microscope (Hitachi SU8010, Japan). The XRD analysis was measured by a

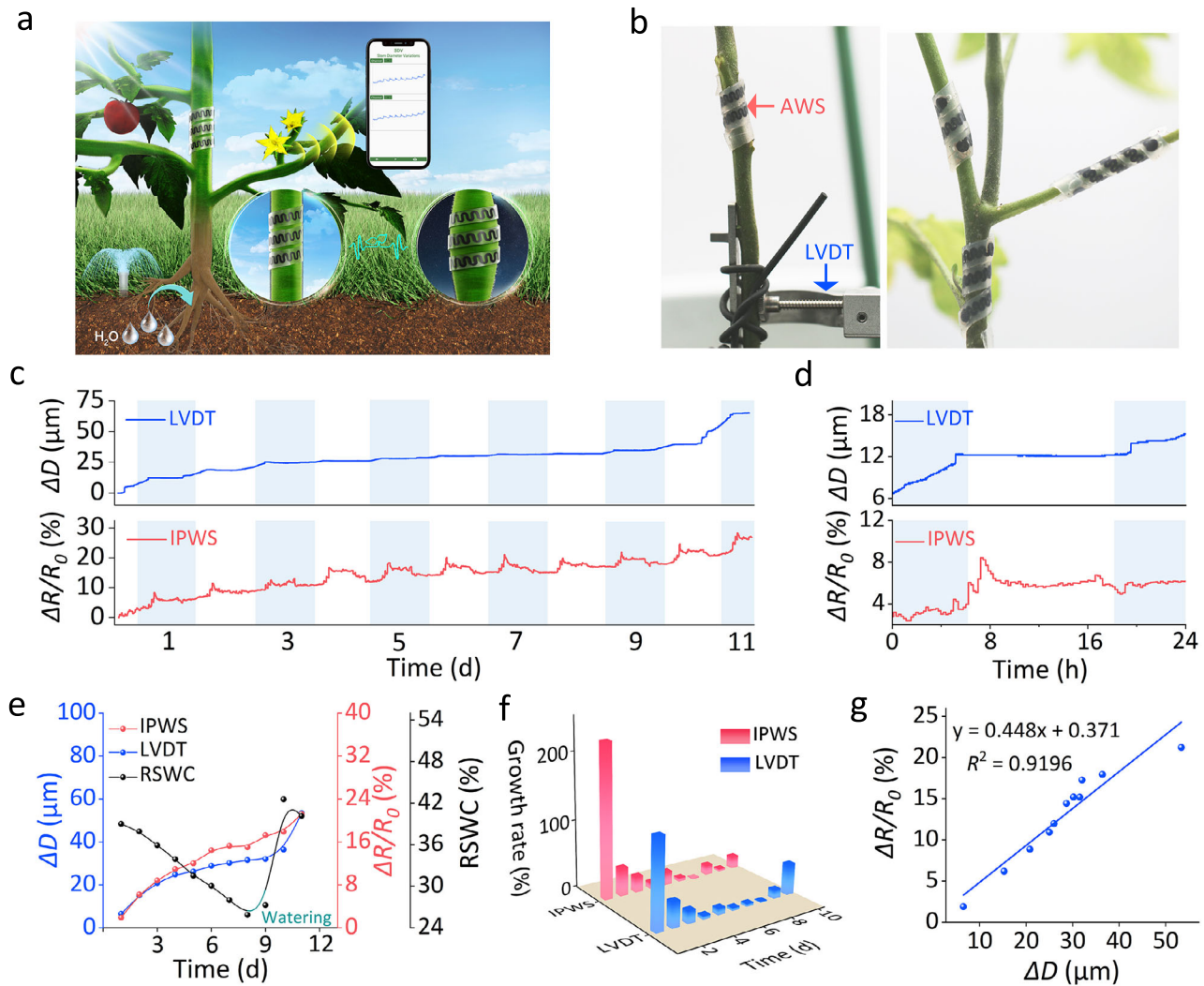


Fig. 6 In vivo monitoring of plant pulse. **a** Schematics of the IPWS for plant pulse monitoring with smartphone for continuous data readout. **b** The optical images of AWS sensor and commercial LVDT sensor on tomato stem. **c** 11 days of monitoring curves obtained from IPWS and reference sensor. **d** The monitoring curves on the 2nd day. **e** The soil moisture data and stem monitoring data. **f** The stem expansion rate measured by the IPWS and reference sensor. **g** The linearity between the SDV measured by the reference sensor and the resistance variation rate measured by IPWS.

D8 advance diffractometer (Bruker, Germany). The Raman spectra characterization was carried out using a Raman microscope system (LabRAM HR Evolution, Horiba Jobin Yvon). A computer-controlled laser scribing micromachining system (Nano Pro-III, Tianjin Jiayin Nanotechnology Co., Ltd., China) was applied to carry out the laser inducing process. Artificial climate box (PRX-1000D) was purchased from Ningbo Safe Experimental Apparatus Co., Ltd, China.

Preparation of PR film

The PR precursor solution consisted with PR and FeCl_3 was prepared as previous reports²⁰. 5 g PR powder were dissolved in 10 mL ethanol, followed by adding 20 mg FeCl_3 and ultrasonic dissolution. The precursor solution should be prepared when it is in need due to the strong hygroscopicity of FeCl_3 . The PR film was prepared on a PDMS substrate. The precursor solution was covered over the entire PDMS substrate, and the homogeneous PR film can be obtained followed by a spin-coating process at a speed of 900 rpm min^{-1} for 40 s. The obtained PR film was dried at room temperature for the following laser inducing procedure.

Fabrication of AWS sensor

The fabrication of AWS sensor contains three procedures. Firstly, the fabrication of LIG. The laser power (2.2, 2.5, and 2.8 W) and laser scan speed

(16, 27, and 80 cm s^{-1}) were used to prepare LIG with different morphologies. The redundant PR film was rinsed with ethanol and water repeatedly to obtain the patterned LIG. Secondly, transferring patterned LIG to the Ecoflex film. Ecoflex liquid precursor silicone was prepared by mixing the component A and B as a ratio of 1:1. The silicone was injected on the surface of patterned LIG with 30 s of equilibrium. A spin coating procedure was applied at a speed of 600 rpm min^{-1} for 60 s to form the homogeneous Ecoflex film. After curing for 1 h at room temperature, the cured Ecoflex film was peeled off carefully to obtain the Ecoflex/LIG structure. The copper wires were pasted on both ends of the patterned LIG with conductive silver paste to form Ecoflex/LIG electrode. Finally, the fabrication of AWS sensor. Ecoflex/LIG electrode was flipped over, and pasted on the prestretched Ecoflex film with prestrain of 0%, 30%, 50%, 100%, and 200%. Back of electrode was encapsulated by spin coating Ecoflex liquid precursor silicone and curing at room temperature to form a sandwich structure. An AWS sensor can be obtained by releasing the prestretched film.

Design and fabrication of the wireless sensing circuit

A circuit on a FPCB was designed and fabricated to realize the wireless communication between the AWS sensor and a smart phone. The system consisted of an AWS sensor, a LDC2214 analog digital converter (ADC), an ESP32 center processing unit (CPU) with WIFI module, and a power source.

The sensor was directly connected to an ADC to transmit the resistance data. The sensing data was then processed through the ESP32 controller and finally transmitted to a smart phone by the inserted WIFI module. This system can be powered by a USB interface or a rechargeable lithium-ion battery (a nominal voltage of 3.6 V).

DATA AVAILABILITY

The data that support the findings of this study are available from the corresponding author upon reasonable request.

Received: 13 December 2021; Accepted: 27 May 2022;

Published online: 13 June 2022

REFERENCES

- Li, Z. et al. Real-time monitoring of plant stresses via chemiresistive profiling of leaf volatiles by a wearable sensor. *Matter* **4**, 2553–2570 (2021).
- Nassar, J. M. et al. Compliant plant wearables for localized microclimate and plant growth monitoring. *npj Flex. Electron.* **2**, 1–12 (2018).
- Tang, W. et al. Rapid fabrication of wearable carbon nanotube/graphite strain sensor for real-time monitoring of plant growth. *Carbon* **147**, 295–302 (2019).
- Tang, W., Yan, T., Ping, J., Wu, J. & Ying, Y. Rapid fabrication of flexible and stretchable strain sensor by chitosan-based water ink for plants growth monitoring. *Adv. Mater. Technol.* **2**, 1700021 (2017).
- Chai, Y. F. et al. Cohabiting plant-wearable sensor in situ monitors water transport in plant. *Adv. Sci.* **8**, 2003642 (2021).
- Abdelfatah, A., Aranda, X., Save, R., de Herralde, F. & Biel, C. Evaluation of the response of maximum daily shrinkage in young cherry trees submitted to water stress cycles in a greenhouse. *Agric. Water Manag.* **118**, 150–158 (2013).
- Wang, X. S. et al. Determination of a suitable indicator of tomato water content based on stem diameter variation. *Sci. Hortic.* **215**, 142–148 (2017).
- Gallardo, M., Thompson, R. B., Valdez, L. C. & Fernandez, M. D. Response of stem diameter variations to water stress in greenhousegrown vegetable crops. *J. Hortic. Sci. Biotechnol.* **81**, 483–495 (2006).
- Gallardo, M., Thompson, R. B., Valdez, L. C. & Fernández, M. D. Use of stem diameter variations to detect plant water stress in tomato. *Irrig. Sci.* **24**, 241–255 (2006).
- Fernández, J. E. & Cuevas, M. V. Irrigation scheduling from stem diameter variations: A review. *Agr. For. Meteorol.* **150**, 135–151 (2010).
- Moreno, F., Conejero, W., Martín-Palomo, M. J., Girón, I. F. & Torrecillas, A. Maximum daily trunk shrinkage reference values for irrigation scheduling in olive trees. *Agric. Water Manag.* **84**, 290–294 (2006).
- Sengupta, D., Romano, J. & Kottapalli, A. G. P. Electrospun bundled carbon nanofibers for skin-inspired tactile sensing, proprioception and gesture tracking applications. *npj Flex. Electron.* **5**, 1–14 (2021).
- Han, S. et al. Multiscale nanowire-microfluidic hybrid strain sensors with high sensitivity and stretchability. *npj Flex. Electron.* **2**, 1–10 (2018).
- Guo, X. G. et al. Controlled mechanical assembly of complex 3D mesostructures and strain sensors by tensile buckling. *npj Flex. Electron.* **2**, 1–7 (2018).
- Chu, Z. et al. A novel wrinkle-gradient strain sensor with anti-water interference and high sensing performance. *Chem. Eng. J.* **421**, 129873 (2021).
- Zhao, Y. C. et al. A wearable freestanding electrochemical sensing system. *Sci. Adv.* **6**, eaaz0007 (2020).
- Wong, S. K. & Chen, K. C. A procedural approach to modelling virtual climbing plants with tendrils. *Comput. Graph. Forum* **35**, 5–18 (2016).
- Wang, W., Li, C., Cho, M. & Ahn, S. H. Soft tendril-inspired grippers: Shape morphing of programmable polymer-paper bilayer composites. *ACS Appl. Mater. Interfaces* **10**, 10419–10427 (2018).
- Cheng, Y. et al. A biomimetic conductive tendril for ultrasensitive and integratable electronics, muscles, and sensors. *ACS Nano* **12**, 3898–3907 (2018).
- Wang, M., Lin, B. P. & Yang, H. A plant tendril mimic soft actuator with photo-tunable bending and chiral twisting motion modes. *Nat. Commun.* **7**, 13981 (2016).
- Fuard, D., Tzvetkova Chevolleau, T., Decossas, S., Tracqui, P. & Schiavone, P. Optimization of poly-di-methyl-siloxane substrates for studying cellular adhesion and motility. *Microelectron. Eng.* **85**, 1289–1293 (2008).
- Zhang, E. N. et al. Mechanically matched silicone brain implants reduce brain foreign body response. *Adv. Mater. Technol.* **6**, 2000909 (2021).
- Wang, L. et al. Highly stretchable, anti-corrosive and wearable strain sensors based on the PDMs/CNTs decorated elastomer nanofiber composite. *Chem. Eng. J.* **362**, 89–98 (2019).
- Greco, F. et al. Ultra-thin conductive free-standing PEDOT/PSS nanofilms. *Soft Matter* **7**, 10642–10650 (2011).
- Park, Y. G., Lee, S. & Park, J. U. Recent progress in wireless sensors for wearable electronics. *Sensors* **19**, 1–34 (2019).
- Lee, Y., Cha, S. H., Kim, Y. W., Choi, D. & Sun, J. Y. Transparent and attachable ionic communicators based on self-cleanable triboelectric nanogenerators. *Nat. Commun.* **9**, 1804 (2018).
- Lorwongtragool, P., Sowade, E., Watthanawisuth, N., Baumann, R. R. & Ker-dcharoen, T. A novel wearable electronic nose for healthcare based on flexible printed chemical sensor array. *Sensors* **14**, 19700–19712 (2014).
- Lee, Y. et al. Wireless, intraoral hybrid electronics for real-time quantification of sodium intake toward hypertension management. *Proc. Natl Acad. Sci.* **115**, 5377–5382 (2018).
- Alam, A. U., Clyne, D., Jin, H., Hu, N. X. & Deen, M. J. Fully integrated, simple, and low-cost electrochemical sensor array for in situ water quality monitoring. *ACS Sens.* **5**, 412–422 (2020).
- Yang, Y. et al. A laser-engraved wearable sensor for sensitive detection of uric acid and tyrosine in sweat. *Nat. Biotechnol.* **38**, 217–224 (2020).
- Stanford, M. G. et al. Laser-induced graphene triboelectric nanogenerators. *ACS Nano* **13**, 7166–7174 (2019).
- Duy, L. X. et al. Laser-induced graphene fibers. *Carbon* **126**, 472–479 (2018).
- Wang, S. et al. Network cracks-based wearable strain sensors for subtle and large strain detection of human motions. *J. Mater. Chem. C* **6**, 5140–5147 (2018).
- Luo, S., Samad, Y. A., Chan, V. & Liao, K. Cellular graphene: Fabrication, mechanical properties, and strain-sensing applications. *Matter* **1**, 1148–1202 (2019).
- Zheng, Q., Lee, J.-H., Shen, X., Chen, X. & Kim, J.-K. Graphene-based wearable piezoresistive physical sensors. *Mater. Today* **36**, 158–179 (2020).
- Torresi, L. et al. Raman investigation of laser-induced structural defects of graphite oxide films. *EPJ Web Conf.* **167**, 04011 (2018).
- Ferrante, C. et al. Raman spectroscopy of graphene under ultrafast laser excitation. *Nat. Commun.* **9**, 308 (2018).
- Zhang, C., Ping, J. F. & Ying, Y. B. Evaluation of trans-resveratrol level in grape wine using laser-induced porous graphene-based electrochemical sensor. *Sci. Total Environ.* **714**, 136687 (2020).
- Zobeiri, H., Hunter, N., Wang, R., Wang, T. & Wang, X. Direct characterization of thermal nonequilibrium between optical and acoustic phonons in graphene paper under photon excitation. *Adv. Sci.* **8**, 2004712 (2021).
- Gao, X. L. et al. Reduced graphene oxide hydrogels prepared in the presence of phenol for high-performance electrochemical capacitors. *N. Carbon Mater.* **34**, 403–415 (2019).
- You, Z. et al. Laser-induced noble metal nanoparticle-graphene composites enabled flexible biosensor for pathogen detection. *Biosens. Bioelectron.* **150**, 111896 (2020).
- Han, Y. et al. Direct growth of highly conductive large-area stretchable graphene. *Adv. Sci.* **8**, 2003697 (2021).
- Lin, J. et al. Laser-induced porous graphene films from commercial polymers. *Nat. Commun.* **5**, 5714 (2014).
- Kurra, N., Jiang, Q., Nayak, P. & Alshareef, H. N. Laser-derived graphene: A three-dimensional printed graphene electrode and its emerging applications. *Nano Today* **24**, 81–102 (2019).
- Feng, J., Zhang, W., Liu, C., Guo, M. & Zhang, C. Homoclinic and heteroclinic orbits in climbing cucumber tendrils. *Sci. Rep.* **9**, 5051 (2019).
- Kha, H., Tumble, S. C., Kalyanasundaram, S. & Williamson, R. E. Wallgen, software to construct layered cellulose-hemicellulose networks and predict their small deformation mechanics. *Plant Physiol.* **152**, 774–786 (2010).
- Wu, S. Y., Peng, S. H., Han, Z. J., Zhu, H. W. & Wang, C. H. Ultrasensitive and stretchable strain sensors based on maze-like vertical graphene network. *ACS Appl. Mater. Interfaces* **10**, 36312–36322 (2018).
- Trung, T. Q. et al. A stretchable strain-insensitive temperature sensor based on free-standing elastomeric composite fibers for on-body monitoring of skin temperature. *ACS Appl. Mater. Interfaces* **11**, 2317–2327 (2019).
- Yang, J. et al. Wearable temperature sensor based on graphene nanowalls. *RSC Adv.* **5**, 25609–25615 (2015).
- Zhang, Z. et al. Visible light laser-induced graphene from phenolic resin: A new approach for directly writing graphene-based electrochemical devices on various substrates. *Carbon* **127**, 287–296 (2018).

ACKNOWLEDGEMENTS

This work was supported by the Joint Funds of the National Natural Science Foundation of China (Grant No. U20A2019).

AUTHOR CONTRIBUTIONS

All authors contributed to the discussion of the results and to the preparation of the manuscript. Chao Zhang, Jianfeng Ping and Yibin Ying conceived the original ideas presented in this work. Chao Zhang conducted the sensor design and fabrication. Chi Zhang and Xinyue Wu conducted the design and fabrication of the wireless sensing circuit. Chao Zhang wrote the manuscript which was further improved by Jianfeng Ping and Yibin Ying.

COMPETING INTERESTS

The authors declare no competing interests.

ADDITIONAL INFORMATION

Supplementary information The online version contains supplementary material available at <https://doi.org/10.1038/s41528-022-00177-5>.

Correspondence and requests for materials should be addressed to Yibin Ying.

Reprints and permission information is available at <http://www.nature.com/reprints>

Publisher's note Springer Nature remains neutral with regard to jurisdictional claims in published maps and institutional affiliations.



Open Access This article is licensed under a Creative Commons Attribution 4.0 International License, which permits use, sharing, adaptation, distribution and reproduction in any medium or format, as long as you give appropriate credit to the original author(s) and the source, provide a link to the Creative Commons license, and indicate if changes were made. The images or other third party material in this article are included in the article's Creative Commons license, unless indicated otherwise in a credit line to the material. If material is not included in the article's Creative Commons license and your intended use is not permitted by statutory regulation or exceeds the permitted use, you will need to obtain permission directly from the copyright holder. To view a copy of this license, visit <http://creativecommons.org/licenses/by/4.0/>.

© The Author(s) 2022